



# Correlating fracture toughness and fracture surface roughness via correlation length scale

Y. Barak · A. Srivastava · S. Osovski 

Received: 16 January 2019 / Accepted: 5 June 2019 / Published online: 19 July 2019  
© Springer Nature B.V. 2019

**Abstract** Fracture toughness of a material depends on its microstructure and the imposed loading conditions. Intuitively, the resultant fracture surfaces must contain the information about the interlacing of these intrinsic (microstructure) and extrinsic (imposed loading) characteristics. Mandelbrot's revelation that fracture surfaces are fractals, excited both the scientific and engineering communities, spurring a series of works focused at correlating the fracture toughness and the fracture surface roughness. Unfortunately, these studies remained inconclusive and later on it was shown that the fractal dimension of the fracture surface roughness is in fact universal. Here, we show that by going beyond the universality, a definite correlation between the fracture toughness and indices of the fracture surface roughness is obtained. To this end, fracture experiments on an aluminum alloy were carried over a wide range of loading rates ( $10^{-2}$ – $10^6$  MPa $\sqrt{\text{ms}^{-1}}$ ), and the resulting fracture surface were reconstructed using stereography. The correlation lengths, extracted from the reconstructed surfaces, were found to be linearly correlated with the measured fracture toughness. The correlation unraveled in our work, along with the proposed mechanistic interpretation, revives the hope

of correlating fracture toughness and fracture surface roughness, allowing quantitative failure analysis and a potential reconstructive approaches to designing fracture resistant materials.

**Keywords** Dynamic fracture · Fracture mechanisms · Fracture toughness · Fracture surface roughness · Mechanical testing

## 1 Introduction

The fracture process in ductile materials, in general involves nucleation, growth and coalescence of micron-scale voids, resulting in relatively greater crack growth resistance. To put this in to perspective, the atomic work of separation for any material is 1–10 J/m<sup>2</sup> (Hayes et al. 2004; Van der Ven and Ceder 2004) whereas the work of crack advance in ductile materials is 10<sup>4</sup>–10<sup>5</sup> J/m<sup>2</sup> (Lautridou and Pineau 1981). The difference comes from the micron and larger scale dissipations associated with the ductile fracture process and lead to highly irregular fracture surfaces. These fracture surfaces are expected to contain the evidence of the influence of both the intrinsic (microstructure) and extrinsic (imposed loading) characteristics of the fracture process. Thus, it is no wonder, that the study of fracture surfaces dates back to the sixteenth century (ASM Metals handbook 1987). However, in the absence of a quantitative geometrical method for characterizing the irregular surfaces, these studies were strictly qual-

Y. Barak · S. Osovski (✉)  
Faculty of Mechanical Engineering, Technion – Israel  
Institute of Technology, Haifa, Israel  
e-mail: osovski.technion@gmail.com

A. Srivastava  
Department of Materials Science and Engineering, Texas A&M  
University, College Station, TX, USA

itative. Nevertheless these qualitative studies helped unravel—micromechanism of ductile fracture, origin of striations in fatigue fracture and cleavage pattern in brittle fracture, to name a few (Pineau et al. 2015, 2016).

The quest for correlating the post mortem analysis of fracture surfaces with the energy invested in their creation gained attention with the technological advancements in the characterization tools and in the description of complex geometries in the twentieth century. In particular, Mandelbrot et al. (1984) were the first to quantitatively characterize the scale invariant properties or fractal nature of the fracture surfaces (Mandelbrot et al. 1984). Mandelbrot et al. (1984) also introduced the fractal dimension of the fracture surfaces as a quantifying parameter that can potentially be correlated with the apparent toughness of the material. This spurred a series of works focused at correlating the fracture toughness and the fracture surface roughness via the fractal dimension (Carney and Mecholsky 2013; Charkaluk et al. 1998; Davidson 1989; Mecholsky et al. 1989; Wang et al. 1988), resulting in contradictory observations ranging from negative, positive or no correlation. This discrepancy is largely due to relatively small variation in the values of the fractal dimension (Bouchaud 1990) and the different methods used to estimate the fractal dimension (Charkaluk et al. 1998). Later on, it was shown that the fractal dimension or the exponent characterizing the scale invariance of the fracture surface roughness is universal, i.e. independent of the material and its toughness (Bonamy and Bouchaud 2011; Bouchaud 1990) as long as the overall fracture mechanism remains the same.

Indeed, the scale invariant properties of fracture surfaces have been observed in a variety of materials, ranging from engineering alloys to composites to geomaterials, and under a variety of loading conditions ranging from quasi-static to fatigue to dynamic fracture (Bouchaud 1997; Charkaluk et al. 1998; Cherepanov et al. 1995; Dauskardt et al. 1990; Underwood and Banerji 1986). The universality of the scaling exponent, and the various theoretical models used to explain it (Bonamy and Bouchaud 2011; Bouchbinder et al. 2004; Ramanathan et al. 1997), do not coincide with the fact that the fracture toughness depends on both the material and the loading conditions, and can vary over orders of magnitude even if the overall fracture mechanism remains the same. The universality of the scaling

exponent thus limits the applicability of statistical analyses of the fracture surfaces for the characterization of the fracture process and fracture toughness.

Recently, we (Osovski et al. 2015; Srivastava et al. 2014) carried out three dimensional calculations of ductile crack growth under mode I small scale yielding conditions with the aim of predicting the variation of crack growth resistance and fracture surface roughness with material microstructure and imposed loading rate. The calculations were carried out using an elasto-viscoplastic constitutive relation for a progressively cavitating solid with two populations of void nucleating second phase particles: small homogeneously distributed particles that nucleate voids at large plastic strains, and discrete large inclusions that result in void nucleation at an early stage of the deformation history. The extent of crack growth in these calculations were sufficient to extract the crack growth resistance parameters and quantify the statistical features of the fracture surface roughness. From the calculations, a quantitative correlation between the correlation length scales beyond which the scale invariant properties of the fracture surface roughness break down, and the material microstructure and loading rate were unraveled. Similar, dependence of correlation length scales on material microstructure were also observed in some experimental works (Hinojosa et al. 1998, 2000; Hinojosa and Aldaco 2002).

Interestingly, in Srivastava et al. (2014) it was found that the variations in the fracture toughness arising from changing the density of the void nucleating large inclusions in the calculations correlate linearly with the correlation length scales extracted from the calculated fracture surface roughness. A similar correlation between the fracture toughness and fracture surface roughness was found in Osovski et al. (2015), for a material with fixed density of large inclusions subjected to varying loading rates. Here, inspired by our previous computational results, we carry out an experimental study to show that indeed by going beyond the universality of the scale invariant properties, a definite correlation between the fracture toughness and the fracture surface roughness can be obtained. In particular, we show that the lateral and vertical correlation lengths, beyond which the scale invariant properties of the fracture surface roughness break down, scale linearly with the fracture toughness.

## 2 Material microstructure and mechanical property

### 2.1 Microstructural characterization

The material examined in this work is an Aluminum alloy (AA) 6061-T6. The AA6061-T6 is a precipitation-hardened alloy with a high magnesium and silicon content. Commercial AA6061-T6 rolled sheets with 1.6 mm thickness were acquired from McMaster-Carr Supply Company. Extensive metallographic studies were performed on the as-received material to determine the material's intrinsic length scales, such as, mean inclusion spacing and grain size. Metallographic specimens of the as-received material were mounted using cold acrylic resin, and then grinded using SiC papers (320 and 1000 grit) with water as lubricant. Next, the specimens were mechanically polished on lapping cloth with 3  $\mu\text{m}$  and 1  $\mu\text{m}$  diamond suspensions. Special care was given throughout all grinding and polishing stages to avoid applying excessive force that may embed the polishing particles into the specimen surface. Finally, the specimens were electropolished using an ethanol-perchloric acid solution. Some of the mechanically polished specimens (prior to electropolishing) were lightly etched using Kroll's reagent. Metallographic analyses were performed using a Tescan Mira-3 FEG-SEM. The surfaces were imaged at a resolution of  $4096 \times 4096$  pixels over a view field of 500  $\mu\text{m}$  resulting in a pixel size of 122 nm. A representative SEM-BSE image of the microstructure of as-received AA6061-T6 showing the distribution of inclusions is shown in Fig. 1.

#### 2.1.1 Mean inclusion spacing

The rolling process leaves behind inclusions shattered into tiny particles along with larger inclusions, Fig. 1. To measure the inclusion size and mean inclusion spacing, we first apply a grayscale binary image thresholding to the SEM-BSE images to separate the inclusions from the background. The size of the tiny particles were found to be  $\sim 0.122 \mu\text{m}^2$  and that of larger inclusions were found to be in the range  $\sim 7\text{--}12 \mu\text{m}^2$  with a few very large inclusions reaching up to  $50 \mu\text{m}^2$ . A large amount of these sub-micron particles, clustered together, has a significant influence on the mean inclusion spacing measurements. Hence, we must somehow

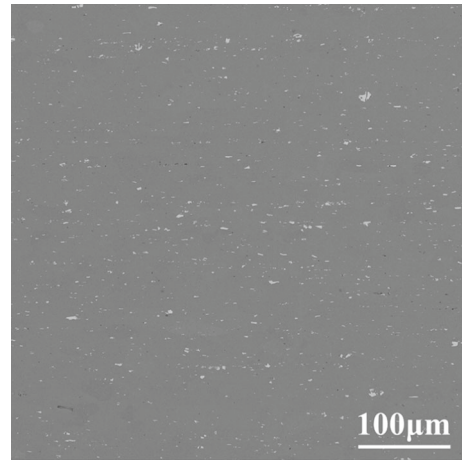


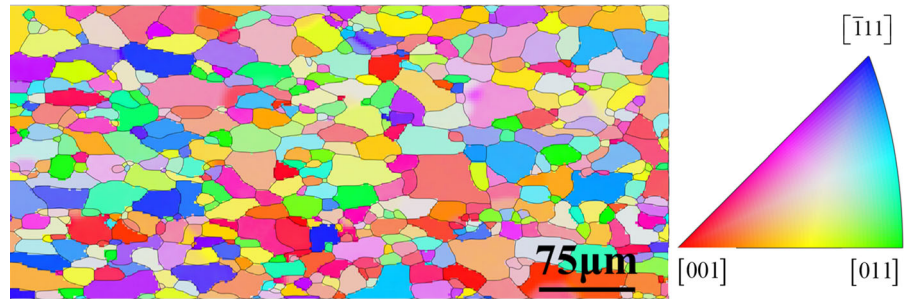
**Fig. 1** SEM-BSE image showing the distribution of inclusions in the as-received AA6061-T6 sheet metal. Large variation in inclusion size and inclusion-inclusion distances are noted

balance the weight of the small and large inclusions when quantifying the mean inclusion spacing. To this end, several algorithms were considered (k-means, user defined size thresholding and nearest neighbors analysis to name a few) to extract the mean inclusion spacing. All of the considered algorithms, were found to be extremely sensitive to the user's input such as number of clusters, threshold inclusion size etc. and failed to successfully balance the weight of large versus small particles in the measurement of the mean inclusion spacing. Following this we relied on the dimensionless geometrical parameter:

$$M(t) = \left\langle \frac{\sqrt{A_i} N(t)}{\hat{L}_i n_i} \right\rangle_i \quad (1)$$

where  $A_i$  is the area of inclusion  $i$ ,  $\hat{L}_i$  is the average distance between centroids of inclusion  $i$  and each of its nearest neighbors,  $n_i$  is the number of nearest neighbors of inclusion  $i$ , and finally,  $N(t)$  is the total number of inclusions for the given threshold  $t$ . The use of the dimensionless geometric parameter in Eq. (1) allows us to assign more weight to larger inclusions without determining a specific threshold. By plotting the variation of  $M(t)$ , we can classify the particles into 5 size groups. Considering the threshold size as the value corresponding to the peak after which there is no trend in the variation of  $M(t)$ , the mean spacing between the inclusions was quantified to be  $l_0 = 30 \mu\text{m}$ .

**Fig. 2** EBSD inverse poll figure map of as-received AA6061-T6 sheet metal. The normal direction of the sheet metal is along the viewing direction



### 2.1.2 Grain size

Metallographic specimens were extracted along all three sheet directions (Rolling, Transverse and Normal directions). The specimens were polished following the standard techniques and subsequently electropolished before being subjected to EBSD analysis using an Oxford EBSD detector. The EBSD pattern was acquired at 20 kV beam voltage and 0.7  $\mu\text{m}$  step size. A representative inverse pole figure map of the as received AA6061-T6 sheet metal is shown in Fig. 2. The line interception method was then used to extract the average grain size along all the three sheet directions. The average grain size through the thickness of the sheet was found to be 15  $\mu\text{m}$  which is roughly half of the mean inclusion spacing.

## 2.2 Mechanical characterization

The uniaxial stress–strain behavior of AA6061-T6 sheet metal along the rolling direction was examined over a range of imposed strain rates varying from 0.001 to 5500  $\text{s}^{-1}$ . Quasi static tests were carried out using an Instron servo-hydraulic machine while the high rate experiments were carried out using a split Hopkinson tension/compression bar (SHTB/SHPB) utilizing C300 hardened Maraging steel bars. Both compression and tension experiments were carried out at high strain rates to better characterize the rate dependent flow response of the material. The tensile specimens were connected to the SHTB using a designated cylindrical specimen clamp fitted to the sheet specimen geometry as shown in the insert in Fig. 3. Two strain gages were glued on each bar and sampled at 2 MHz using a Nicolet 450 oscilloscope. The measured signals were used to obtain the force–displacement curves, which were then converted to nominal stress–strain curves shown in Fig. 3. On an

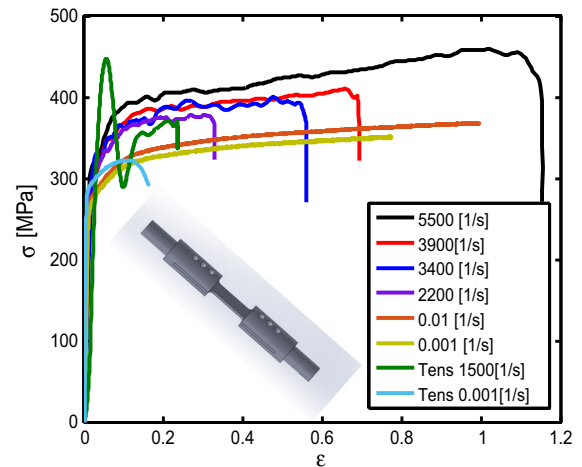


**Fig. 3** The experimentally obtained quasi-static and dynamic uniaxial nominal stress strain curves. The curves labelled, Tens, are obtained from tension tests while the other curves are obtained from compression tests. The insert shows the cylindrical specimen clamp fitted to the sheet specimen geometry for tension tests

average, in the quasi-static regime the observed yield stress  $\sigma_y^s \approx 270$  MPa while in the dynamic regime the observed yield stress  $\sigma_y^d \approx 300$  MPa. Furthermore, the strain rate sensitivity of the material is found to vary over the deformation history with the strain rate sensitivity exponent being  $\sim 0.014$  for flow stress taken at the onset of plastic deformation whereas the exponent is  $\sim 0.025$  for flow stress taken at a strain of 0.1. Due to extensive ringing in the signals obtained for tension at strain rates,  $\dot{\epsilon} > 1500 \text{ s}^{-1}$ , only compression curves are presented for higher strain rates.

## 3 Fracture toughness

Double edge notched tensile (DENT) specimens with the axis aligned parallel to the rolling direction of the



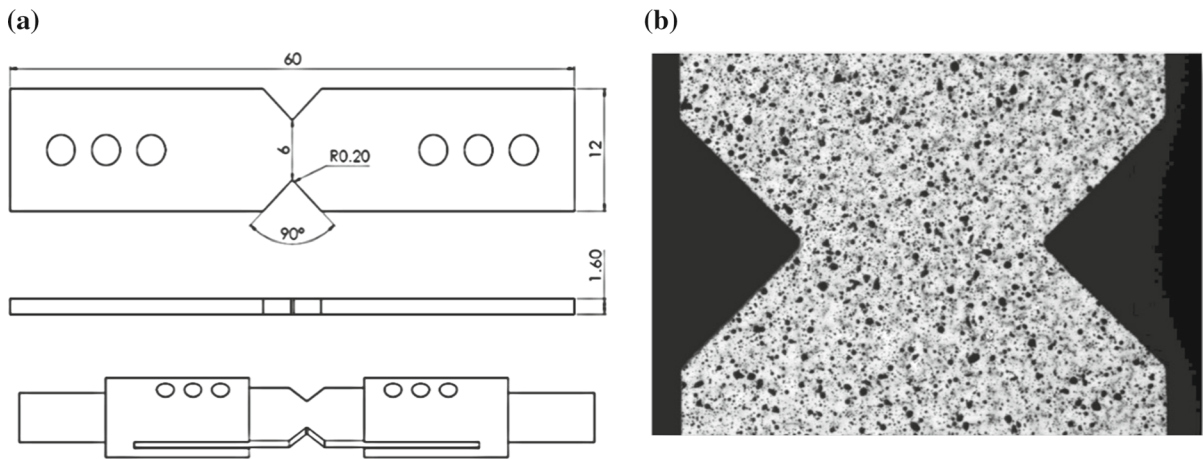


**Fig. 4** **a** Geometry and dimensions of the double edge notch tension specimen used for fracture experiments. **b** Random speckle pattern on a double edge notch specimen

as-received sheets of AA6061-T6 were machined using electro-discharged machining. The DENT geometry is shown in Fig. 4a. The fracture tests using DENT specimens were carried out at velocities ranging from  $4 \times 10^{-7}$  m/s to 16 m/s resulting in imposed rate of the mode I stress intensity factor ranging from  $\dot{K}_I \approx 10^{-2}$  MPa $\sqrt{\text{m/s}}$  to  $\dot{K}_I \approx 10^6$  MPa $\sqrt{\text{m/s}}$ . To cover this large range of loading rates, we used two experimental setups: (i) Standard Instron load frame to characterize the fracture toughness in the quasi-static regime; and (ii) A split Hopkinson tensile bar to characterize the fracture toughness in the dynamic regime. Prior to conducting the experiments, the specimens were coated with a random speckle pattern consisting of black and white paint (Fig. 4b). Special care was taken to ensure that the white layer of coating was not continuous as in early attempts a continuous layer of white color resulted in debonding of the coating from the specimen's surface under high loading rates. The quasi-static tests were imaged using an allied vision camera recording at 30 fps, while the high rate experiments were continuously imaged using a Kirana high-speed camera capturing 180 frames with  $\sim 1$  megapixel resolution at 1 million fps (Crooks et al. 2013).

The digital image correlation (DIC) technique was used to obtain full field displacements/strains throughout the experiment using the “Match ID” software with a pixel size of 0.01–0.03 mm. The displacement field obtained from the DIC measurements were used to measure the crack tip opening displacement (CTOD),

$\delta$ . Fracture toughness was then measured based on the relation between  $\delta$ ,  $K$  and  $J$  (Rice 1968):

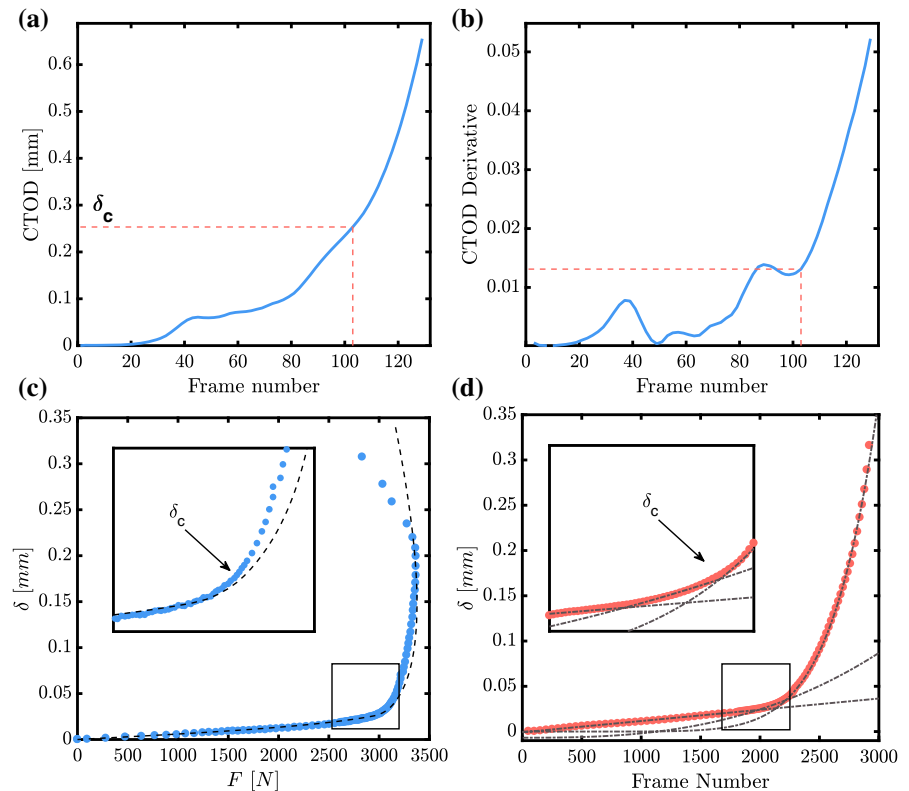
$$\begin{aligned} K_I &= \sqrt{J E} = \sqrt{m \sigma_y E} \sqrt{\delta} \\ \dot{K}_I &= \frac{1}{2} \sqrt{m \sigma_y E} \delta^{-1/2} \dot{\delta} \end{aligned} \quad (2)$$

The value of the CTOD at crack growth initiation,  $\delta_c$ , was then used to estimate the fracture toughness (Shih 1981),  $J_{IC} = m \sigma_y \delta_c$ , of the material, where  $m$  is taken to be 1 due to the plane stress conditions and  $\sigma_y$  is the yield strength of the material corresponding to the respective strain rate regime.

To determine the critical value of  $\delta$  (i.e. the value at crack growth initiation— $\delta_c$ ) one needs to identify very precisely the exact moment of crack growth initiation. To avoid large errors in the values of  $\delta_c$ , arising from mis-identification of the crack growth initiation time, three separate methods were applied.

Method 1 takes advantage of the derivative of  $\delta$  with respect to time throughout the experiment. It is assumed that once a crack starts propagating, the value of  $\delta$  will increase rapidly. Therefore, the frame where the derivative increases rapidly is considered as the frame of initiation and  $\delta_c$  is the value of  $\delta$  measured in this frame, Fig. 5a, b. Methods 2 and 3 are both based on the assumption that the measured mechanical response can be divided into three regimes, the first is linear elastic, followed by a regime which is governed by plasticity without any crack growth and finally crack growth takes place. In method 2, the experiments were simulated using a commercial finite element software (Abaqus\Explicit) using the experimentally measured

**Fig. 5** **a** The value of  $\delta$  as measured from the DIC analysis versus the frame number. **b** The time derivative of  $\delta$  as measured from the DIC analysis versus the frame number. **c** A comparison between the evolution of  $\delta$  as a function of the reaction force ( $F$ ) measured from the experiment (dashed line) and extracted from the finite element simulation (dotted line). The separation between the curves is used to identify the value of  $\delta_c$  (insert in **c**). **d** The measured  $\delta$  values (dotted line) and the three fitting regimes (dashed lines). The intersection of the second and third fitting curves is denoted as  $\delta_c$  (insert in **d**)



material properties shown in Fig. 3. The numerical simulations were carried out within the framework of  $J_2$  isotropic elasto-viscoplastic formulation using the full kinematics as to account for the large deformation near the notch tip. A power law material model was used:

$$\sigma_{flow} = \left( \sigma_y^0 + k (\varepsilon_p)^n \right) \left( \frac{\dot{\varepsilon}}{\dot{\varepsilon}_0} \right)^m \quad (3)$$

with  $\sigma_{flow}$  being the flow stress and  $\sigma_y^0 = 270$  MPa being the yield stress at the reference strain rate,  $\dot{\varepsilon}_0 = 0.001$  s<sup>-1</sup>. The hardening coefficient  $k = 358$  MPa, hardening exponent  $n = 0.054$  and rate sensitivity exponent  $m = 0.014$  were calibrated to fit the experimental data. No damage model was used and therefore the simulations do not account for crack initiation and propagation. In the first two regimes (purely elastic deformation followed by the beginning of plastic flow), the experiment and the simulation are expected to correlate quantitatively. However, once a crack will start to grow, a breakdown in the correlation is expected. Thus, while comparing the experiment and the simulation it is expected that the curves will separate upon crack initiation. The value of  $\delta$  at this separation is simply the  $\delta_c$ . An example of the data analysis using this

method is given in Fig. 5c for the case of quasi-static loading. Finally, method 3 used curve fitting. A linear fit was used for the elastic regime and two power law fits were used for the second (plastic flow) and the third regimes (the crack growth regime). Using this method, initiation is considered at the intersection of the second and third regime fits, see Fig. 5d. The critical CTOD values extracted from all three methods were found to be in good agreement with each other. The final critical CTOD ( $\delta_c$ ) used to estimate the fracture toughness ( $J_{IC}$ ) is the mean value of the  $\delta_c$  obtained using the three methods.

The variation in the fracture toughness,  $J_{IC}$ , with imposed loading rate,  $\dot{K}_I$ , is shown in Fig. 6. Here we note, that the reported values of  $\dot{K}_I$  are estimated using Eq. (2) and therefore are just an approximation at the late stages of deformation where extensive plasticity is present. As shown in the figure, the fracture toughness of the material in the quasi-static regime is not very sensitive to the changes in the applied loading rate whereas in the dynamic regime the fracture toughness of the material strongly depends on the applied loading

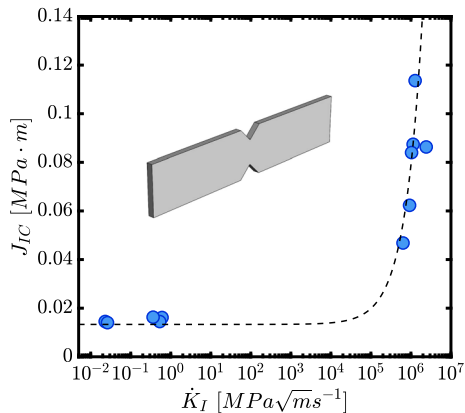


**Fig. 6** The variation of measured fracture toughness ( $J_{IC}$ ) as a function of the imposed loading rate,  $\dot{K}_I$ . Here, both the fracture toughness ( $J_{IC}$ ) and the rate of increase in the mode I stress intensity factor ( $\dot{K}_I$ ) were extracted from the measured CTOD

rate. Similar observation was made for Al-2024 alloy by Owen et al. (1998).

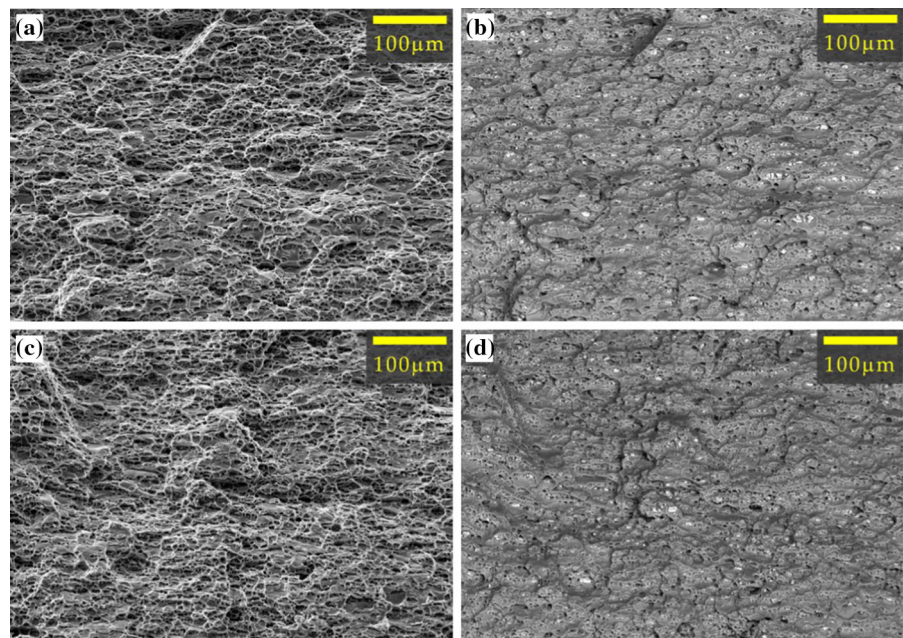
#### 4 Fracture surfaces

The representative SEM-SE images of the fracture surfaces of AA6061-T6 sheet metal presented in Fig. 7a, c, show dimples on the fracture surface, which indicates a ductile fracture mechanism governed by the

nucleation, growth and coalescence of micron scale voids. In the SEM-BSE images, Fig. 7b, d, inclusions can be observed within the dimples, highlighting their role in the void nucleation process. The fracture surfaces shown in Fig. 7a, b are representative for low loading rates ( $\dot{K}_I \approx 2.4 \times 10^{-2}$  MPa $\sqrt{m}$ /s) while Fig. 7c, d are representative for high loading rate ( $\dot{K}_I \approx 6.5 \times 10^5$  MPa $\sqrt{m}$ /s). Similar images taken from all of the reported specimens confirm that the fracture mechanism does not depend on the loading rate.

To quantitatively characterize the highly irregular ductile fracture surfaces shown in Fig. 7, we first digitized the experimental fracture surfaces. To achieve this we captured several  $600 \times 600 \mu\text{m}^2$  regions of a fracture surface using a SE detector in the TESCAN MIRA3 FEG-SEM, at two tilt angles,  $3^\circ$  from each other, with a resolution of  $0.1465 \mu\text{m}$  per pixel. The 3D fracture surfaces and digital elevation maps were then recreated using stereographic reconstruction in the “Mountains-Map” software suite by “Digital-Surf”. A typical recreated fracture surface of dimension  $600 \times 600 \mu\text{m}^2$  corresponding to a specimen fractured at an applied loading rate of  $\dot{K}_I \approx 6.5 \times 10^5$  MPa $\sqrt{m}$ /s is shown in Fig. 8a. Next, from each fracture surface we extract 100 equidistant line profiles of the variation in the out-of-plane height ( $h$ ) of the fracture surface along the crack propagation direction ( $x$ ) and calculate

**Fig. 7** **a** Representative SEM-SE image of fracture surface of a double edge notch tension specimen deformed at a loading rate of  $\dot{K}_I \approx 2.4 \times 10^{-2}$  MPa $\sqrt{m}$ /s. The SEM-BSE image of the region in **a** is shown in **b**. **c** Representative SEM-SE image of fracture surface of a double edge notch tension specimen deformed at a loading rate of  $\dot{K}_I \approx 6.5 \times 10^5$  MPa $\sqrt{m}$ /s. The SEM-BSE image of the region in **c** is shown in **d**



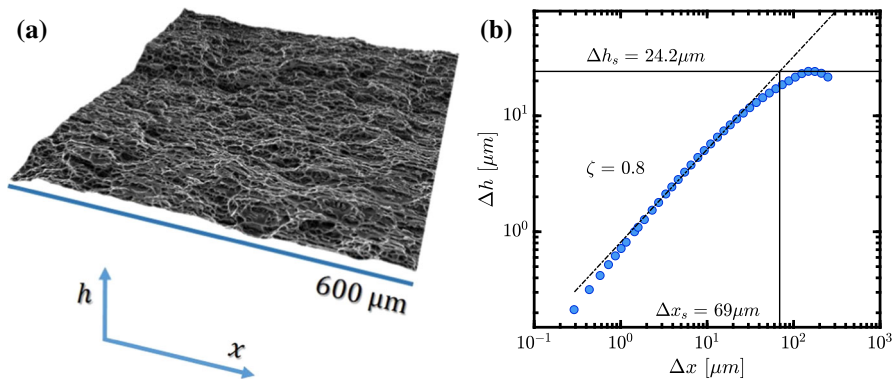


**Fig. 8** **a** A 3D stereographic reconstruction of a  $600 \times 600 \mu\text{m}^2$  region extracted from the fracture surface of a specimen loaded at  $\dot{K}_I \approx 6.5 \times 10^5 \text{ MPa}\sqrt{\text{m/s}}$ . The pixel size is  $0.1465 \mu\text{m}$ . **b** The

height-height correlation function of the surface in **a**. The universal scaling exponent ( $\beta$ ), the lateral correlation length ( $\Delta x_s$ ) and its associated height ( $\Delta h_s$ ) are marked in the figure

the height-height correlation function:

$$\Delta h(\Delta x) = \sqrt{\langle [h(x + \Delta x) - h(x)]^2 \rangle_{x,n}} \propto (\Delta x)^\beta \quad (4)$$

where  $h$  is the height at a location  $x$  along the crack propagation direction,  $\beta$  is the scaling (Hurst) exponent and  $\langle \rangle_{x,n}$  denotes average over  $x$  and  $n$ , with  $n$  being the number of line profiles. In Eq. (4), the quantity  $\Delta h(\Delta x)$  is simply the typical difference of heights between two points separated by a distance  $\Delta x$ . The minimum value of  $\Delta x$  i.e.  $\Delta x_{\min}$  is determined by the resolution of the digital elevation map. The value of Hurst exponent,  $\beta$ , in Eq. (1), necessarily lies between 0 and 1 where  $\beta = 0$  corresponds to a straight line with slope zero and  $\beta = 1$  corresponds to a straight line with a nonzero slope. The value  $\beta = 0.5$  correspond to a random walk suggesting no correlation between  $\Delta h$  and  $\Delta x$ . The value of  $\beta > 0.5$  indicate persistence i.e. an increase (decrease) in  $\Delta h$  with increasing  $\Delta x$  will most likely be followed by an increase (decrease) with further increase in  $\Delta x$ . The value of  $\beta < 0.5$ , on the other hand, indicate anti-persistence (or mean reverting) i.e. an increase (decrease) will be followed by a decrease (increase) or in other words  $\Delta h$  has the tendency to revert to a mean value with increasing  $\Delta x$ .

A typical log-log plot of the correlation function obtained using  $\Delta x_{\min} = 0.1465 \mu\text{m}$  is shown in Fig. 8b. The correlation function in Fig. 8b is for the fracture surface shown in Fig. 8a. We note that the correlation functions obtained using  $\Delta x_{\min} = 0.1465 \mu\text{m}$  along the crack propagation direction for all the cases were found to be statistically invariant. In addition, irrespective of the applied loading rate,  $\dot{K}_I$ , the correlation func-

tions exhibit a power law scaling,  $\Delta h(\Delta x) \propto (\Delta x)^\beta$ , with  $\beta$  varying within a narrow range of 0.76 to 0.82 across all tested specimens, regardless of the loading rate and measured value of the fracture toughness. The value of  $\beta$  or the Hurst exponent for all the cases was calculated as the slope of the line fitted to the range,  $2.6 \mu\text{m} < \Delta x < 26 \mu\text{m}$ , on the log-log plot, as shown in Fig. 8b. The insensitivity of the Hurst exponent for the range of applied loading rate considered, is in-line with the universality of the exponent characterizing the scale invariance of the fracture surface roughness. The value of  $\beta > 0.5$  indicates persistence, which is also in-line with the fact that irrespective of the applied loading rate a growing crack has the tendency to continue growing, at least for a while, in the same direction.

As can be seen from Fig. 8b, if the value of  $\beta$  is calculated as the slope of the line fitted to small values of  $\Delta x$  i.e.  $\Delta x < 2.6 \mu\text{m}$ , the value of  $\beta$  is greater than the value obtained as the slope of the line fitted to the range,  $2.6 \mu\text{m} < \Delta x < 26 \mu\text{m}$ . In order to understand the scaling of the correlation function at small length scales, we analyzed the fracture surface at a magnification approximately 20 times greater than the one used in Fig. 8a. A typical fracture surface of dimension  $30 \times 30 \mu\text{m}^2$  ( $\Delta x_{\min} = 0.0073 \mu\text{m}$ ) extracted from a specimen fractured at a loading rate of  $\dot{K}_I \approx 1.0 \times 10^6 \text{ MPa}\sqrt{\text{m/s}}$  is shown in Fig. 9a. The height-height correlation function along the crack propagation direction extracted from two  $30 \times 30 \mu\text{m}^2$  regions of the same fracture surface are shown in Fig. 9b. It



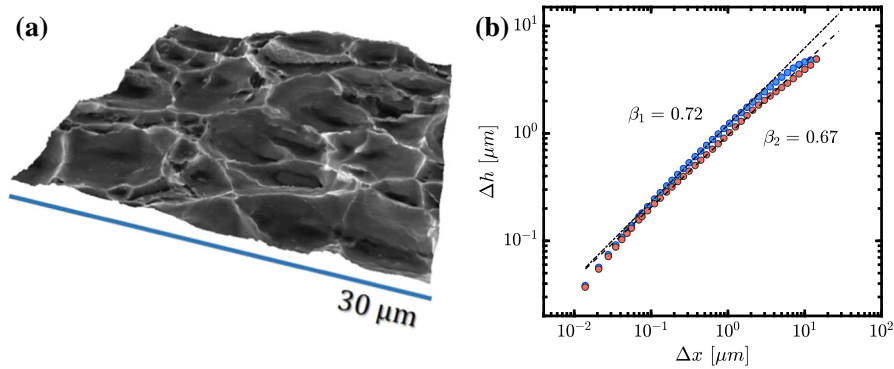


**Fig. 9** **a** A 3D stereographic reconstruction of a  $30 \times 30 \mu\text{m}^2$  region extracted from the fracture surface of a specimen loaded at  $\dot{K}_I \approx 1.0 \times 10^6 \text{MPa}\sqrt{\text{m}}/\text{s}$ . The pixel size is  $0.0073 \mu\text{m}$ . **b** The height-height correlation function of the surface in **a** and a

second region of the same size take from a different location on the fracture surface. The scaling exponent extracted from both regions are marked in the figure

was found that the correlation function obtained from  $30 \times 30 \mu\text{m}^2$  regions are not statistically invariant over the fracture surface. Both the correlation functions in Fig. 9b do exhibit power law scaling but with different values of the Hurst exponent,  $\beta$ . In addition, similar to Fig. 8b, here as well for small values of  $\Delta x$  the local slope of both the curves is still greater than their respective Hurst exponents. First, the fact that the correlation function obtained from the high magnification fracture surface using  $\Delta x_{\min} = 0.0073 \mu\text{m}$  is not statistically invariant is simply because of the non-uniform nucleation and growth of voids in the material within the limited field of view in high magnification images. Second, the fact that for small values of  $\Delta x$ , the local slope of the curve is still greater than the value of the Hurst exponent, is a result of the stereographic reconstruction algorithm, which uses an  $8 \times 8$  pixel window to spatially correlate points between the tilted images which limits the applicability of this method when  $\Delta x$  approaches the pixel size. In Bonamy et al. (2006) it was predicted that the Hurst exponent may obtain different values depending on the size of the region over which it is extracted. For regions that are smaller than the process zone, a value of  $\sim 0.5$  is expected while a value of  $\sim 0.6$ – $0.7$  was predicted for a transition zone (i.e. when the size of the sampled region is comparable with the process zone size). Those predictions were later on observed experimentally for glass in (Hinojosa et al. 2008). Here we note that the values of the Hurst exponent extracted from the  $30 \times 30 \mu\text{m}^2$  regions were all in the range of  $0.64$ – $0.73$ , while the values of

the Hurst exponent extracted from the  $600 \times 600 \mu\text{m}^2$  regions were  $0.8 \pm 0.03$ . Thus, the height-height correlation function at a scale comparable to the intrinsic length scale of the material i.e. mean inclusion spacing ( $l_0 = 30 \mu\text{m}$ ) is very sensitive to the sampling region and hence we recommend to focus on a length scale which is larger than  $l_0$  for the analysis of the fracture surface roughness.

Next, note that for large values of  $\Delta x$ , the local slope of the curve in Fig. 8b is less than the Hurst exponent and it further decreases with increasing  $\Delta x$ . For large enough  $\Delta x$  the local slope eventually goes to zero. The value of the local slope of the height-height correlation function below  $0.5$  indicates anti-persistence. Anti-persistence at large values of  $\Delta x$  is because, at large length scales, the growing crack tends to revert back to the mean fracture plane, despite the attraction it feels from the randomly distributed inclusions. Furthermore, the value of  $\Delta x$  at which the local slope of the correlation function goes to zero indicates the lateral correlation length ( $\Delta x_s$ ) at which the height-height correlation function is (nearly) constant and the surface features are no longer correlated. Our rigorous analysis of the scale invariant properties of the fracture surface roughness of the specimens tested over a range of applied loading rates clearly show that the Hurst exponent,  $\beta$ , cannot provide a quantitative correlation between the fracture toughness and fracture surface roughness as it was envisioned in the past.

Nevertheless, as evident from Fig. 7, the observed variation in fracture toughness with the applied loading

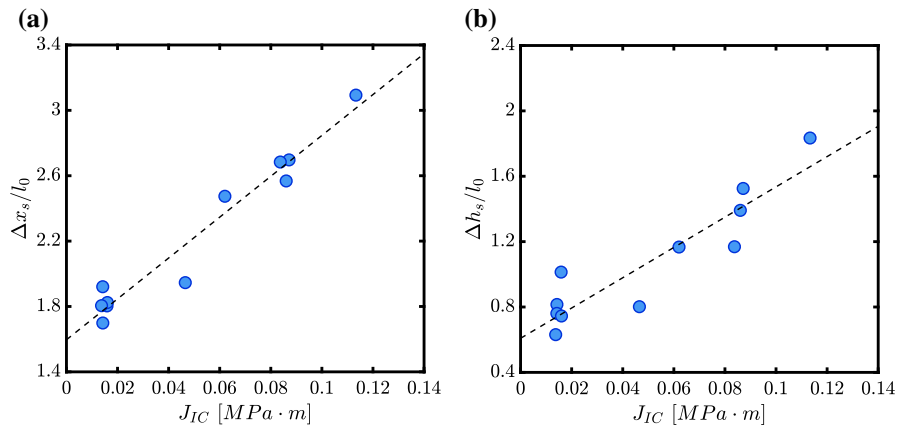


**Fig. 10** Correlating the fracture toughness with length scales extracted from the fracture surface roughness: A linear correlation between the two characterizing parameters of the fracture surface roughness and the fracture toughness is found. **a** The variation of the normalized lateral correlation length,  $\Delta x_s/l_0$ —

representing the in-plane roughness with the fracture toughness,  $J_{IC}$ . **b** The variation of the normalized corresponding height,  $\Delta h_s/l_0$ —representing the out of plane roughness with the fracture toughness,  $J_{IC}$

rate is not due to any variation in the micromechanism of ductile fracture. Instead, the toughness increases due to the increase in the spread of damage (fracture process zone size) and plastic dissipation (plastic zone size) ahead of the crack tip with increasing loading rate (Osovski et al. 2015). As the loading rate increases, the region in which the stress level is sufficient to trigger void nucleation spreads further away from the crack tip (due to the material's rate sensitivity), allowing for more damage sites to interact with one another (Broberg 1979). This process may not affect the nature of crack meandering that dictates the universality of the scale invariant properties of the fracture surface roughness. But it must affect the extent of it that dictates the lateral correlation length ( $\Delta x_s$ ). We postulate that the distance over which voids interact will manifest itself on the fracture surface roughness in such a way that it will dictate the value of  $\Delta x_s$ , as was previously observed numerically (Osovski et al. 2015; Srivastava et al. 2014). Following this, we go beyond the universality of the scale invariant properties of the fracture surface roughness and extract two characterizing parameters,  $\Delta h_s$  and  $\Delta x_s$ . The value of  $\Delta h_s$  is the maximum value of the correlation function,  $\Delta h(\Delta x)$ , and the value of  $\Delta x_s$  is the value of  $\Delta x$  at the intersection of  $\Delta h(\Delta x) = \Delta h_s$  and the line fit to the linear portion of the log–log plot as illustrated in Fig. 8b. The values of  $\Delta x_s$  and  $\Delta h_s$  quantify the extent of crack meandering. In a previous work, it was demonstrated

that the correlation length extracted from a sinusoidal crack indeed return the sinus wave length and the corresponding height (denoted as  $\Delta h_s$ ) reflects the sinus amplitude (Srivastava et al. 2017). The variations of  $\Delta x_s$  and  $\Delta h_s$  with fracture toughness,  $J_{IC}$ , are shown in Fig. 10a, b. The values of  $\Delta x_s$  and  $\Delta h_s$  in Fig. 10 are normalized with the microstructural length scale,  $l_0$ . For low loading rates, where variations in the fracture toughness were relatively small (Fig. 6) the points are clustered together, however, with increasing loading rate, as the material becomes tougher, the values of  $\Delta x_s$  and  $\Delta h_s$  increase linearly. The linear dependence of  $\Delta x_s$  and  $\Delta h_s$  on  $J_{IC}$  can be rationalized by assuming that the extent of crack meandering depends on the size of the volume in which inclusions are activated to play their role as void nucleation sites. The experimental results, summarized in Fig. 10, are in direct agreement with our previously published roughness–toughness correlations obtained from numerical simulations (Osovski et al. 2015; Srivastava et al. 2014).

## 5 Discussion

The universality of the scaling exponents of fracture surfaces has attracted a lot of interest since its discovery. However, it has failed to provide a quantitative tool for the post mortem analysis of fracture surfaces. By going beyond this universality, and extracting the correlation length from the fracture surface, we were able

to demonstrate a linear relation between the measured fracture toughness and the fracture surface roughness. Although the correlation length of fracture surfaces has been studied (Hinojosa et al. 1998, 2000; Hinojosa and Aldaco 2002) and shown to yield the microstructural length scale associated with the fracture process, we are not aware of any experimental effort so far to correlate its variation with the variation in fracture toughness. Our results indicate that this correlation, when studied over a variety of microstructures and loading scenarios, can manifest into a quantitative tool for failure analysis. The attractiveness of the method we propose lies in the fact that, unlike previous sought after correlations (Carney and Mecholsky 2013; Mandelbrot et al. 1984; Wang et al. 1988), it is not purely empirical but rather originates from a mechanistic approach.

The quantitative correlation between the fracture toughness with length scales extracted from the fracture surface roughness presented here are for a specific alloy. Nevertheless, we note that the continuum scale simulations carried out using a constitutive framework for a progressively cavitating isotropic elastic-viscoplastic material (Osovski et al. 2015; Srivastava et al. 2014) containing two populations of void nucleating particles, have demonstrated similar correlations between the numerically obtained fracture surfaces and fracture toughness. A direct comparison between the previously published numerical results and the experimental data presented here is not straightforward, as the numerical model was not calibrated for a specific material. Nonetheless, several similarities are noted. In particular, the values of  $\Delta x_s$  extracted from the numerical results of Srivastava et al. (2014) for low inclusion densities and under quasi-static loading conditions, scale linearly with  $l_0$  with a slope of  $\sim 2$ , and in our experiments, for quasi-static loading conditions, on an average  $\Delta x_s/l_0$  is  $\sim 1.8$ . Also, for both, the experiments (current work) and the numerical simulations (Osovski et al. 2015), for a fixed  $l_0$  and varying imposed loading rates,  $\Delta h_s/l_0$  and  $J_{IC}$  exhibit a linear correlation. Following this, we can claim generality at least for ductile materials undergoing fracture by void nucleation, growth and coalescence.

For ductile structural materials used in engineering applications, of course, the fracture processes can be more complex. For example, cleavage can occur in ligaments between two voids under extreme conditions. Even restricting attention to void nucleation, growth and coalescence induced crack growth, the frac-

ture process in certain polycrystalline structural metals and alloys can be dominated by voids that nucleate and grow preferentially along grain boundaries. The fracture toughness of a material indeed depends on the material properties, active fracture mechanisms, microstructural length scales and loading conditions. Intuitively, these in turn will affect the fracture surface roughness and the analysis presented here can be extended to probe such effects.

Whilst the work presented here aims primarily at elucidating the correlation between fracture toughness and fracture surface roughness, this has broader scientific implications. For example, it can serve in validating existing theories regarding the size and evolution of the process zone and its relation to the intrinsic and extrinsic characteristics of the fracture process. The understanding of the interlacing between the microstructure and the imposed loading and its effect on the fracture toughness and damage tolerance is essential for designing toughness oriented new materials. The modern data analysis tools (e.g. machine learning) can be trained to perform quantitative fractography once a large enough data set is available covering different classes of materials and loading scenarios. These can then be used as a potential reconstructive approaches to designing fracture resistant materials.

## 6 Concluding remarks

We have carried out fracture experiments using double edge notch tension specimens of an aluminum alloy over a wide range of loading rates,  $\dot{K}_I$ , varying from  $10^{-2}$ – $10^6$  MPa $\sqrt{\text{m/s}}$ . The fracture toughness of the material as a function of the imposed loading rate were quantified and the resulting fracture surfaces were reconstructed using stereography. The reconstructed fracture surfaces were then used to extract indices of the fracture surface roughness.

The key conclusions of this work are:

1. The value of the Hurst exponent,  $\beta$ , is found to be constant over the entire range of the loading rate considered, in agreement with the universal value ( $\beta \approx 0.8$ ).
2. The value of the lateral correlation length scale,  $\Delta x_s$ , and the maximum value of the correlation function,  $\Delta h_s$ , extracted from the fracture surface roughness are found to increase with the increasing loading rate, in agreement with the hypothesis

that the fracture process zone size increases with the increasing loading rate that in turn increases the crack tortuosity.

3. A linear correlation is found between the two indices of the fracture surface roughness,  $\Delta x_s$  and  $\Delta h_s$ , and the fracture toughness of the material over the entire range of the loading rate considered.

**Acknowledgements** We thank Dr. Alan Needleman of Texas A&M University and Dr. Daniel Rittel of Technion – Israel Institute of Technology for helpful and stimulating discussions. The financial support provided by the Pazy foundation Young Researchers Award (Grant No. 1176) and European Union's Horizon2020 Program (Excellent Science, Marie-Sklodowska-Curie Actions, H2020 - MSCA - RISE - 2017) under REA grant agreement 777896 (Project QUANTIFY) is gratefully acknowledged.

## References

- ASM Metals Handbook (1987) Fractography. vol 12. ASM International Metals Park, Ohio, USA
- Bonamy D, Bouchaud E (2011) Failure of heterogeneous materials: a dynamic phase transition? *Phys Rep* 498:1–44
- Bonamy D, Ponson L, Prades S, Bouchaud E, Guillot C (2006) Scaling exponents for fracture surfaces in homogeneous glass and glassy ceramics. *Phys Rev Lett* 97:1–5
- Bouchaud E (1990) Fractal dimension of fractured surfaces : a universal value? *Fractal Dimens Eur Phys Lett* 13:73
- Bouchaud E (1997) Scaling properties of cracks. *J Phys Condens Matter* 9:4319
- Bouchbinder E, Mathiesen J, Procaccia I (2004) Roughening of fracture surfaces: the role of plastic deformation. *Phys Rev Lett* 92:245505–1
- Broberg KB (1979) On the behaviour of the process region at a fast running crack tip. In: Kawata K, Shioiri J (eds) *High velocity deformation of solids*. Springer, Berlin, pp 182–194
- Carney LR, Mecholsky JJJ (2013) Relationship between fracture toughness and fracture surface fractal dimension in AISI 4340 steel. *Mater Sci Appl* 4:258–267
- Charkaluk E, Biggerelle M, Iost A (1998) Fractals and fracture. *Eng Fract Mech* 61:119–139
- Cherepanov GP, Balankin AS, Ivanova VS (1995) Fractal fracture mechanics—a review. *Eng Fract Mech* 51:997–1033
- Crooks J, Marsh B, Turchetta R, Taylor K, Chan W, Lahav A, Fenigstein A (2013) Kirana: a solid-state megapixel uCMOS image sensor for ultrahigh speed imaging. In: *Sensors, cameras, and systems for industrial and scientific applications XIV*, p 865903
- Dauskardt RH, Haubensak F, Ritchie RO (1990) On the interpretation of the fractal character of fracture surfaces. *Acta Metall Mater* 38:143–159
- Davidson DL (1989) Fracture surface roughness as a gauge of fracture toughness: Al-particulate SiC Composites. *J Mater Sci* 24:681–687
- Hayes RL, Ortiz M, Carter EA (2004) Universal binding-energy relation for crystals that accounts for surface relaxation. *Phys Rev B* 69:172104
- Hinojosa M, Aldaco J (2002) Self-affine fracture surface parameters and their relationship with microstructure in a cast aluminum alloy. *J Mater Res* 17:1276–1282
- Hinojosa M, Bouchaud E, Nghiem B (1998) Long distance roughness of fracture surfaces in heterogeneous materials. *MRS Proc* 539:203–208
- Hinojosa M, Aldaco J, Ortiz U, González V (2000) Roughness exponent of the fracture surface of an Al–Si alloy. *Alum Trans* 3:53–57
- Hinojosa M, Reyes-melo E, Guerra C, González V, Ortiz U (2008) Scaling properties of slow fracture in glass: from deterministic to irregular topography. *Int J Fract* 151:81–93
- Lautridou JC, Pineau A (1981) Crack initiation and stable crack growth resistance in A508 steels in relation to inclusion distribution. *Eng Fract Mech* 15:55–71
- Mandelbrot BB, Passoja DE, Paullay AJ (1984) Fractal character of fracture surfaces of metals. *Nature* 308:721–722
- Mecholsky JJ, Passoja DE, Feinberg-Ringel KS (1989) Quantitative analysis of brittle fracture surfaces using fractal geometry. *J Am Ceram Soc* 72:60–65
- Osovski S, Srivastava A, Ponson L, Bouchaud E, Tvergaard V, Ravi-Chandar K, Needleman A (2015) The effect of loading rate on ductile fracture toughness and fracture surface roughness. *J Mech Phys Solids* 76:20–46
- Owen D, Zhuang S, Rosakis A, Ravichandran G (1998) Experimental determination of dynamic crack initiation and propagation fracture toughness in thin aluminum sheets. *Int J Fract* 90:153–174
- Pineau A, Benzerga AA, Pardoën T (2016) Acta materialia failure of metals I: brittle and ductile fracture. *Acta Mater* 107:424–483
- Pineau A, McDowell DL, Busso EP, Antolovich SD (2016) Failure of metals II: Fatigue. *Acta Materialia* 107:484–507
- Ramanathan S, Ertas D, Fisher DS (1997) Quasistatic crack propagation in heterogeneous media. *Phys Rev Lett* 79:873
- Rice JR (1968) A path independent integral and the approximate analysis of strain concentration by Notches and Cracks. *J Appl Mech* 35:379
- Shih CF (1981) Relationships between the J-integral and the crack opening displacement for stationary and extending cracks. *J Mech Phys Solids* 29:305–326
- Srivastava A, Ponson L, Osovski S, Bouchaud E, Tvergaard V, Needleman A (2014) Effect of inclusion density on ductile fracture toughness and roughness. *J Mech Phys Solids* 63:62–79
- Srivastava A, Osovski S, Needleman A (2017) Engineering the crack path by controlling the microstructure. *J Mech Phys Solids* 100:1–20. <https://doi.org/10.1016/j.jmps.2016.12.006>
- Underwood EE, Banerji K (1986) Fractals in fractography. *Mater Sci Eng* 80:1–14
- Van der Ven A, Ceder G (2004) Thermodynamics of decohesion. *Acta Mater* 52:1223–1235
- Wang ZG, Chen DL, Jiang XX, Ai SH, Shih CH (1988) Relationship between fractal dimension and fatigue threshold value in dual-phase steels. *Scr Metall* 22:827–832

**Publisher's Note** Springer Nature remains neutral with regard to jurisdictional claims in published maps and institutional affiliations.